Torque Control of IPMSM in the Field-Weakening Region With Improved DC-Link Voltage Utilization

Sung-Yoon Jung, Chunting Chris Mi, *Fellow, IEEE*, and Kwanghee Nam, *Member, IEEE*

***Abstract*—In the field weakening region, the voltage is utilized to the maximum to minimize the current amplitude. In this paper, the hexagonal voltage limit is considered to increase the voltage and to decrease the current, as a result to reduce the copper loss. At first, an intersection between the hexagonal voltage limit and torque curve was found. Because the intersection lies on the boundary of the hexagon, the equations of the sides of the hexagon were derived. Since the hexagonal voltage limit rotates in the synchronous reference frame, they are a function of the rotor position. Finally, the voltage angle was calculated from the intersection. To reduce the torque ripple, d-axis current feedback was added to the voltage angle. In the simulation and experiment results, an increase of voltage and a decrease of current were observed. In addition, an improvement of the motor and inverter efficiencies was also achieved.**

***Index Terms*—DC-link voltage utilization, field weakening control, hexagonal voltage limit, interior permanent-magnet synchronous motor (IPMSM), torque control.**

I. Introduction

BECAUSE of drastic improvement of permanent-magnet material, interior permanent-magnet synchronous motors (IPMSMs) have been in the limelight for the last decade in many industrial applications, such as vacuum pumps, machine tools and automation systems, etc. In particular, in electrical vehicles (EVs) and hybrid EVs (HEVs), the IPMSM is the most exclusive candidate for the traction motor due to its high power density, performance, efficiency, and wide operating range. Most IPMSMs for EVs/HEVs are designed to focus on the field weakening region for compactness. Usually, the maximum speed is three or four times higher than the rated speed [1]. A negative d-axis current extends the available speed range, as well as produces an additional torque named by a reluctance torque. Therefore, an optimal combination of d- and q-axis current is crucial for high-speed torque control in the IPMSMs.

Feedforward control is the most common method in the industry to get fast torque response and reduce steady-state error of torque [2]. Lookup tables for d- and q-axis current are constructed for a given torque with respect to various operating conditions, such as dc-link voltage, rotor speed, magnet temperature, etc. In [2], separate lookup tables for d- and q-axis inductance and permanent-magnet flux linkage covering the entire current operating range are used when generating optimal current reference. This method makes up for inaccurate feedforward control owing to motor parameter variation. However, it increases the burden of making new tables for the inductance and permanent-magnet flux linkage.

To remove or simplify the lookup tables, analytic approaches based on the voltage model in the synchronous frame were shown in [3] and [4]. The general solution of the quartic equation was used to get the minimum d- and q-axis current in the whole speed region [3]. To reduce the computational burden, an approximated equation based on flux variables was used in [4]. However, these algorithms are still difficult to implement in real-time applications.

In the direct torque control (DTC), voltage vectors are directly handled to control the torque, as well as the flux without the current controller. Therefore, it has faster torque dynamics and less parameter dependence than the current vector control [5], [6]. However, the torque ripple and unfixed switching frequency have been issues. To solve these problems, Ren *et al.* obtained the duty ratio of the active voltage vector to reduce the torque variation depending on the machine angular velocity [7]. Mathapati and Bocker found optimal hysteresis bands to get the minimum harmonics in the motor currents [8]. Tang *et al.* utilized the space vector modulation (SVM) instead of the hysteresis comparator and the switching table [9]. Preindl and Bolognani applied the model predictive control (MPC) to the DTC [10]. The model input was restricted to a finite set of voltage vectors to limit the switching frequency. While these methods solve the aforementioned problems, the advantages of the original DTC (e.g., simple control structure and parameter independence) are diminished.

In the field weakening region, the maximum voltage, which an inverter can produce with the limited dc-link voltage, is utilized to minimize the copper loss. Therefore, the voltage angle becomes the sole control variable in the torque control based on the voltage vector. The voltage angle was determined

Manuscript received July 21, 2014; revised September 20, 2014; accepted October 12, 2014. Date of publication November 11, 2014; date of current version May 8, 2015.

S.-Y. Jung and C. C. Mi are with the Department of Electrical and Computer Engineering, University of Michigan, Dearborn, MI 48109-2122 USA (e-mail: sungyj@umich.edu; mi@ieee.org).

K. Nam is with the Department of Electronic and Electrical Engineering, Pohang University of Science and Technology (POSTECH), Pohang 790-784, Korea (e-mail: kwnam@postech.ac.kr).

Color versions of one or more of the figures in this paper are available online at http://ieeexplore.ieee.org.

Digital Object Identifier 10.1109/TIE.2014.2369453

by the integration of the q-axis current error in [11] and the torque error in [12]. The d-axis current feedback is added to the aforementioned integrator to improve the stability problem [11], [12]. To increase the maximum torque and motor efficiency, some authors proposed methods to utilize the outside of the linear modulation range in the field weakening region. In [13], the d-axis current reference is adjusted by controlling the voltage trajectory to move to the hexagon of the space vector. The voltage vector within a linear modulation range was scaled to the hexagonal voltage limit to increase dc-link voltage utilization [14]. However, a relation between the scaled voltage and torque was not proven.

In this paper, the torque control method based on the voltage vector in the field weakening region is proposed with better utilization of the dc-link voltage. An equation determining the voltage vector, which is an intersection between the hexagonal voltage limit, and the torque curve, is derived. Since the hexagonal voltage limit rotates in the synchronous reference frame, the derived equation is a function of the rotor position, as well as the torque reference. To reduce the torque ripple induced by the transient voltage, d-axis current feedback is added to the voltage angle. Increased voltage utilization results in lesser current consumption and improves the motor and inverter efficiencies finally. Through the simulation and experiment results, the effectiveness and practicality of the proposed method are validated.

II. IPMSM Model

Equations of steady-state voltage of the IPMSM in the synchronous frame neglecting an ohmic loss across a stator resistance are given by

$$v_d = -\omega_e L_q i_q \tag{1}$$

$$v_q = \omega_e L_d i_d + \omega_e \psi_m \tag{2}$$

where v_d, v_q, i_d, i_q, L_d, and L_q are the d- and q-axis voltage, current, and inductance in the synchronous frame, respectively; ψ_m is the rotor flux linkage, and ω_e is the electrical angular frequency. The electrical torque equation is described by

$$T = \frac{3}{4}P\left(\psi_m i_q + (L_d - L_q) i_d i_q\right) \tag{3}$$

where P is a pole number. By inserting (1) and (2) into (3), the torque equation on the $v_d - v_q$ plane is obtained as

$$v_q = -\frac{4T}{3P} \cdot \frac{\omega_e^2 L_d L_q}{L_d - L_q} \cdot \frac{1}{v_d} - \omega_e \psi_m \cdot \frac{L_q}{L_d - L_q}. \tag{4}$$

Fig. 1 shows the voltage limits and constant torque curves depicted in the voltage plane (v_d, v_q). Within the linear modulation range, the radius of the voltage limit is $(1/\sqrt{3})V_{\mathrm{dc}}$ where V_{dc} is the dc-link voltage. It is marked with the circular voltage limit in Fig. 1. Including the nonlinear modulation range, the voltage limit is extended to a hexagon whose side length is $(2/3)V_{\mathrm{dc}}$, as indicated in Fig. 1. The constant torque appears in the left half as hyperbolas extending vertically.

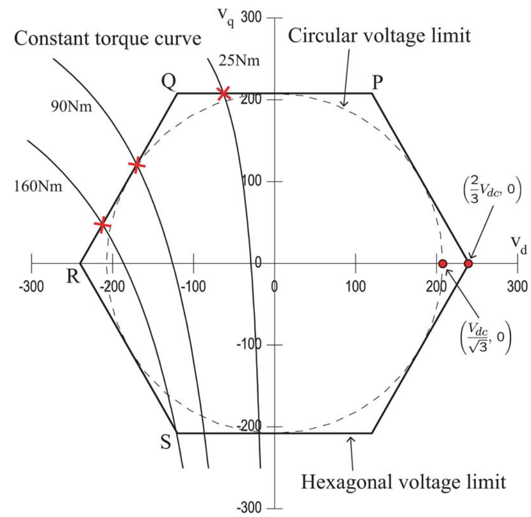

Fig. 1. Hexagonal and circular voltage limit with constant torque curve in the synchronous $d-q$ voltage plane.

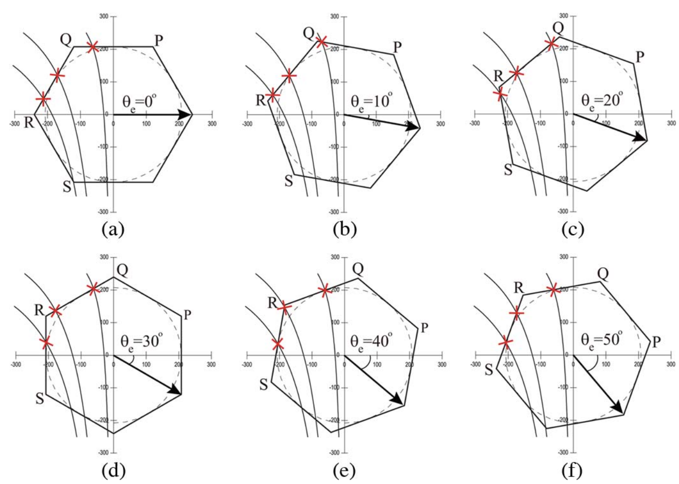

Fig. 2. Rotating hexagonal voltage limit according to the rotor angle, θ_e in the synchronous reference frame: (a) $\theta_e = 0°$. (b) $\theta_e = 10°$. (c) $\theta_e = 20°$. (d) $\theta_e = 30°$. (e) $\theta_e = 40°$. (f) $\theta_e = 50°$.

III. Relation Between Voltage Vector and Torque in the Rotating Hexagon

In [3], the author found an optimal operating point under the current and voltage limit for minimizing the current. In particular, the intersection of the circular voltage limit, and the constant torque curve was the solution in the field weakening region. In this paper, the circular voltage limit is replaced with the hexagonal one. As shown in Fig. 1, each torque curve intersects the hexagon at two points. It should be noted that the current limit appears as an ellipse whose center is $(0, \omega_e\psi_m)$ in the synchronous $d-q$ voltage plane. Therefore, the intersection yielding shorter current vector is the upper one if ω_e is positive. The length of it is longer than the intersection with the circular voltage limit, which means the dc-link voltage utilization is improved compared with [3].

Fig. 2 shows six still shots of the hexagon according to the rotor angle θ_e in the synchronous reference frame. Note that the hexagon rotates clockwise, whereas the rotor rotates counterclockwise. In the meantime, the intersections marked with a red cross also move according to θ_e. Since a hexagon has six rotational symmetries, a trace of the intersection is repeated every 60°; thus, θ_e from 0° to 60° is considered to find the intersection, as shown in Fig. 2. Points P, Q, R, and S, according to θ_e, are given by

$$P = \frac{2}{3}V_{\mathrm{dc}}\begin{bmatrix}\cos\left(\frac{\pi}{3}-\theta_e\right)\\ \sin\left(\frac{\pi}{3}-\theta_e\right)\end{bmatrix} \quad Q = \frac{2}{3}V_{\mathrm{dc}}\begin{bmatrix}\cos\left(\frac{2\pi}{3}-\theta_e\right)\\ \sin\left(\frac{2\pi}{3}-\theta_e\right)\end{bmatrix}$$

$$R = \frac{2}{3}V_{\mathrm{dc}}\begin{bmatrix}\cos(\pi-\theta_e)\\ \sin(\pi-\theta_e)\end{bmatrix} \quad S = \frac{2}{3}V_{\mathrm{dc}}\begin{bmatrix}\cos\left(\frac{4\pi}{3}-\theta_e\right)\\ \sin\left(\frac{4\pi}{3}-\theta_e\right)\end{bmatrix}.$$

The equations of $\overline{PQ}$, $\overline{QR}$, and $\overline{RS}$ are derived as follows:

$$\overline{PQ}: v_q = -\tan\theta_e v_d + \tan\theta_e \cdot \frac{2}{3}V_{\mathrm{dc}} \cdot \cos\left(\frac{\pi}{3}-\theta_e\right) + \frac{2}{3}V_{\mathrm{dc}}\cdot\sin\left(\frac{\pi}{3}-\theta_e\right) \tag{5}$$

$$\overline{QR}: v_q = \tan\left(\frac{\pi}{3}-\theta_e\right)v_d - \tan\left(\frac{\pi}{3}-\theta_e\right)\cdot\frac{2}{3}V_{\mathrm{dc}} \cdot \cos\left(\frac{2\pi}{3}-\theta_e\right) + \frac{2}{3}V_{\mathrm{dc}}\cdot\sin\left(\frac{2\pi}{3}-\theta_e\right) \tag{6}$$

$$\overline{RS}: v_q = \tan\left(\frac{2\pi}{3}-\theta_e\right)v_d - \tan\left(\frac{2\pi}{3}-\theta_e\right)\cdot\frac{2}{3}V_{\mathrm{dc}} \cdot \cos(\pi-\theta_e) + \frac{2}{3}V_{\mathrm{dc}}\cdot\sin(\pi-\theta_e). \tag{7}$$

Inserting (5) into (4), the intersection on $\overline{PQ}$, (v_{d1}, v_{q1}) is derived as (8), shown at the bottom of the page, where α_1 and β_1 are the slope and y-component of $\overline{PQ}$. Since the constant torque curve is a hyperbola, two intersections exist on each line, as seen in (8). Among the two signs, one within the hexagonal voltage limit is the solution. Let V_{m1} be the voltage limit at (v_{d1}, v_{q1}), and it is given by

$$V_{m1} = \frac{V_{\mathrm{dc}}}{\sqrt{3}}\cdot\frac{1}{\cos\left(\mathrm{mod}\left(\theta_r, \frac{\pi}{3}\right)-\frac{\pi}{6}\right)} \tag{9}$$

where $\theta_r = \theta_e + \arctan(v_{q1}/v_{d1})$ and "mod" is the modulo function, which takes a remainder after dividing by $(\pi/3)$ [15].

IV. Torque Control Based on Voltage Angle

Fig. 3 shows the flowchart of the voltage vector selection algorithm for the torque control. For a given torque reference, T^* and rotor position, i.e., θ_e, the goal is to find the voltage vector, (v_d^*, v_q^*) on the boundary of the hexagonal voltage limit.

In the first step, a reminder of θ_e divided by $(\pi/3)$ is calculated. Since it is not known which side of the hexagonal voltage limit intersects with the torque curve, all of the intersections with $\overline{PQ}$, $\overline{QR}$, and $\overline{RS}$ are found using (8). Note that

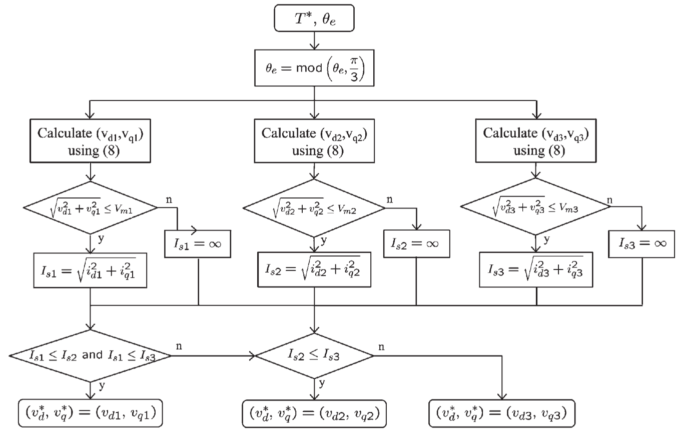

Fig. 3. Flowchart of the voltage vector selection algorithm

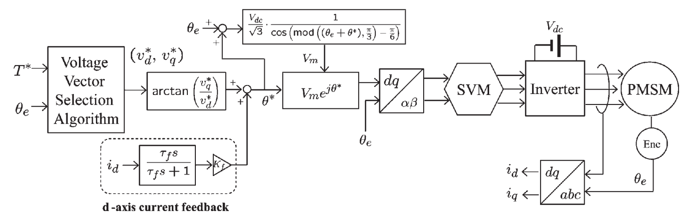

Fig. 4. Block diagram for the torque control with the voltage vector selection algorithm.

(v_{d2}, v_{q2}) and (v_{d3}, v_{q3}) are the intersections with $\overline{QR}$ and $\overline{RS}$, respectively. They are obtained in the same way as when getting (v_{d1}, v_{q1}). Then, each intersection is compared with the voltage limit. Note that V_{m2} and V_{m3} are the voltage limits at (v_{d2}, v_{q2}) and (v_{d3}, v_{q3}), which are derived in the same way of getting V_{m1}. If they are within the voltage limit, an amplitude of the steady-state current vector is calculated as in the following:

$$I_{s1} = \sqrt{i_{d1}^2 + i_{q1}^2} = \sqrt{\left(\frac{v_{q1} - \omega_e\psi_m}{\omega_e L_d}\right)^2 + \left(\frac{v_{d1}}{\omega_e L_q}\right)^2} \tag{10}$$

where (i_{d1}, i_{q1}) is the current vector induced from (v_{d1}, v_{q1}). Note that (i_{d2}, i_{q2}) and (i_{d3}, i_{q3}) are the current vectors induced from (v_{d2}, v_{q2}) and (v_{d3}, v_{q3}) and I_{s2} and I_{s3} are the amplitudes of (i_{d2}, i_{q2}) and (i_{d3}, i_{q3}), respectively. Otherwise, each of the current amplitude is adjusted to infinity to exclude from the candidates of the final solution. At the end, the voltage vector, which has the smallest current vector, is chosen as the final solution.

The overall torque control block diagram is shown in Fig. 4. It contains the voltage vector selection algorithm shown in Fig. 3. The voltage vector selection algorithm generates the reference voltage vector, (v_d^*, v_q^*) without a current controller. There is an additional feedback loop indicated by the d-axis current feedback in Fig. 4. After filtering out high-frequency

$$(v_{d1}, v_{q1}) = \left(\frac{-\beta_1(L_d - L_q) - L_q\omega_e\psi_m \pm \sqrt{(\beta_1(L_d-L_q) + L_q\omega_e\psi_m)^2 - \frac{16T}{3P}\alpha_1\omega_e^2 L_d L_q(L_d - L_q)}}{2\alpha_1(L_d - L_q)}, \alpha_1 v_{d1} + \beta_1\right) \tag{8}$$

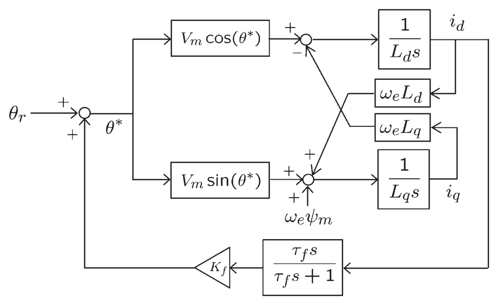

Fig. 5. Block diagram for voltage angel control.

components of the d-axis current and multiplying a filter gain, K_f, the output of the d-axis feedback is added to the angle of (v_d^*, v_q^*). This loop enhances the stability of the torque control loop based on the voltage angle [11], [12].

Let θ^* be the modified voltage angle, and it is calculated as in the following:

$$\theta^* = \arctan\left(\frac{v_q^*}{v_d^*}\right) + K_f \cdot \mathrm{HF}(i_d) \tag{11}$$

where "HF" means a high-pass filter whose time constant is τ_f. Since the additional feedback term changes the voltage angle, the voltage amplitude is recalculated depending on the hexagonal voltage limit at $(\theta_e + \theta^*)$. The final voltage vector for the SVM is calculated as in the following:

$$V_m e^{j\theta^*} = \frac{V_{\mathrm{dc}}}{\sqrt{3}} \cdot \frac{1}{\cos\left(\mathrm{mod}\left((\theta_e + \theta^*), \frac{\pi}{3}\right) - \frac{\pi}{6}\right)} e^{j\theta^*} \tag{12}$$

where V_m is the voltage limit at $(\theta_e + \theta^*)$.

A. Effect of d-Axis Current Feedback

To show how the filter gain, K_f and the time constant of a high-pass filter, τ_f in the d-axis current feedback make the torque response stable, the root locus is plotted. Fig. 5 is the block diagram of the voltage angle control, which only shows the control flow from the voltage angle reference, i.e., θ_r to the d-axis current. The state equations of the forward path are derived as

$$\begin{bmatrix} \dot{i}_d \\ \dot{i}_q \end{bmatrix} = \begin{bmatrix} \frac{\omega_e L_q}{L_d} i_q + \frac{V_m}{L_d} \cos\theta^* \\ -\frac{\omega_e \psi_m}{L_q} - \frac{\omega_e L_d}{L_q} i_d + \frac{V_m}{L_q} \sin\theta^* \end{bmatrix}. \tag{13}$$

Since (13) has nonlinear terms, a linearization around the operating point is needed. The linearized state equation of (13) is

$$\Delta\dot{\mathbf{x}} = \begin{bmatrix} 0 & \frac{L_q}{L_d}\omega_e \\ -\frac{L_d}{L_q}\omega_e & 0 \end{bmatrix} \Delta\mathbf{x} + \begin{bmatrix} -\frac{V_m}{L_d} \sin\theta_0^* \\ \frac{V_m}{L_q} \cos\theta_0^* \end{bmatrix} \Delta u \tag{14}$$

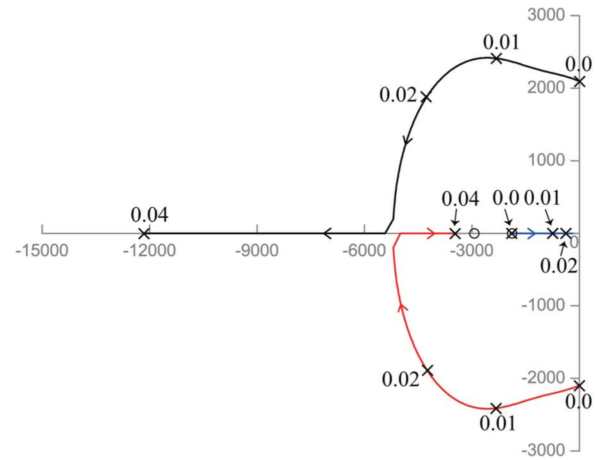

(a)

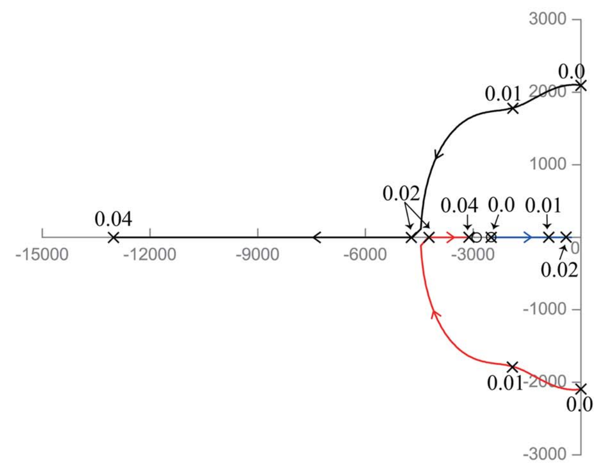

(b)

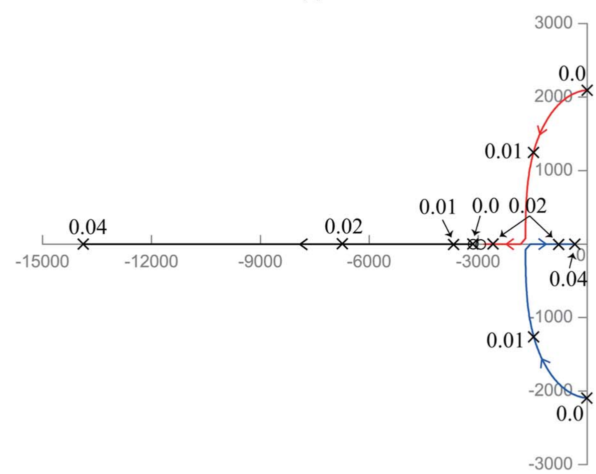

(c)

Fig. 6. Root loci of the voltage angle control loop when K_f varies from 0 to 0.04: (a) $\tau_f = 0.00053$ (300 Hz). (b) $\tau_f = 0.0004$ (400 Hz). (c) $\tau_f = 0.0003318$ (500 Hz).

$$\frac{\Delta i_d}{\theta_r} = \frac{\frac{V_m}{L_d}\left(-\tau_f \sin\theta_0^* \cdot s^2 + (\tau_f \omega_e \cos\theta_0^* - \sin\theta_0^*)\, s + \omega_e \cos\theta_0^*\right)}{\tau_f \cdot s^3 + \left(1 + K_f \tau_f \frac{V_m}{L_d} \sin\theta_0^*\right) s^2 + \left(\omega_e^2 \tau_f - K_f \tau_f \frac{\omega_e}{L_d} V_m \cos\theta_0^*\right) s + \omega_e^2} \tag{16}$$

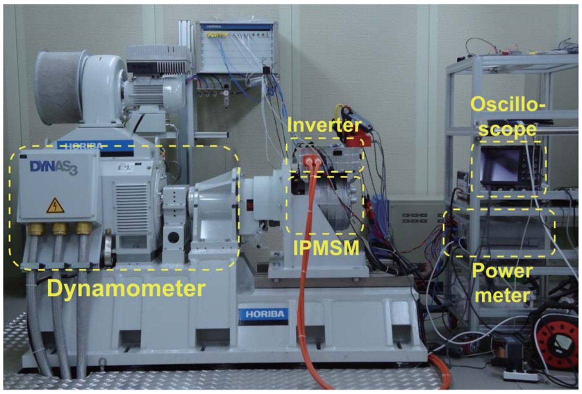

Fig. 7. Experimental equipment: dynamometer, IPMSM, inverter, power meter, and oscilloscope.

where $\Delta\mathbf{x} = [\Delta i_d \;\; \Delta i_q]^T = [i_d - i_{d0} \;\; i_q - i_{q0}]^T$ and $\Delta u = \theta^* - \theta_0^*$. In addition, i_{d0}, i_{q0}, and θ_0^* are the coordinates of an operating point. Based on (14), a forward path transfer function is derived as

$$\frac{\Delta i_d}{\Delta u} = \frac{V_m}{L_d\left(s^2+\omega_e^2\right)} \cdot \left(-\sin\theta_0^* \cdot s + \omega_e \cos\theta_0^*\right). \qquad (15)$$

The closed-loop transfer function, including the d-axis current feedback is shown by (16) at the bottom of the previous page. Note that K_f is shown only in the denominator, whereas τ_f appears in the numerator as well as the denominator. Fig. 6 is the root loci of (16) when K_f varies from 0 to 0.04 and τ_f is 0.00053, 0.0004, and 0.0003318, which correspond to 300, 400, and 500 Hz in the cut off frequency of the high-pass filter, respectively. When $K_f = 0$, in other words, the d-axis current feedback is not working, two complex conjugate poles are located at the imaginary axis in all τ_f. It causes an oscillation in the current and torque response, which is shown in Fig. 8. When $K_f = 0.1$, two complex conjugate poles have both real and imaginary components and less overshoot is expected in the case of Fig. 6(b) compared with the one of Fig. 6(a). In Fig. 6(c), the imaginary parts of the complex conjugate poles are less than the one of Fig. 6(b) at $K_f = 0.1$; however, the real parts are closer to the origin. As shown in Fig. 9, when $\tau_f = 0.0004$ and $K_f = 0.1$, moderate overshoot and rise time are obtained without torque and current oscillation. When K_f increases up to 0.2, all the poles are on the real axis; however, the dominant pole approaches to the origin, as shown in Fig. 6(b); therefore, the torque response is deteriorated.

V. Simulation and Experimental Results

To prove practicality and effectiveness of the proposed torque control algorithm, simulations and experiments were performed. For the simulation, MATLAB Simulink was used to implement the block diagram shown in Fig. 4. It was also realized in a real-time platform, and a dynamometer shown in Fig. 7 was utilized to get the experiment data. The RMS values of voltage and current of the inverter and dc-link were measured via a power meter and the instant value of torque and speed was gathered through the sensors installed in the dynamometer. In addition, all the data are logged to a PC to calculate the efficiency of the motor and inverter. A 100-kVA inverter was used, the switching frequency was 8 kHz, the dead time was 2 μs, and the SVM and minimum phase over modulation were also applied [15]. Table I lists the parameters of the IPMSM used in the simulation, as well as the experiment.

TABLE I
IPMSM Parameters

Variable	Value
Number of poles (P)	8
Maximum speed	12000 RPM
Maximum power	70.0 kW
Maximum torque	185 Nm
Maximum current (I_s)	250.0 A (rms)
DC-link voltage (V_{DC})	360 V
Permanent magnet flux (ψ_m)	0.1046 Wb
Nominal d-axis ind. (L_d)	0.349 mH
Nominal q-axis ind. (L_q)	0.806 mH

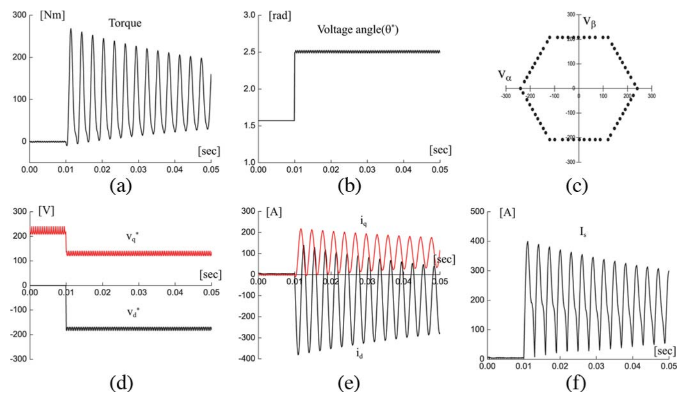

Fig. 8. Stepwise torque response (0 $\rightarrow$ 100 N $\cdot$ m) at 5000 r/min without the negative d-axis current feedback: (a) torque, (b) voltage angle(θ^*), (c) $\alpha\beta$-axis voltage, (d) dq-axis voltage, (e) dq-axis current, and (f) current amplitude.

The goal of the simulations and experiments is to show higher utilization of dc-link voltage; and therefore, the results should show that current consumption is decreased; and finally, energy efficiency is improved compared with the existing current vector control.

A. Simulation Results

From Figs. 8–10, stepwise torque responses are shown when the IPMSM spins at 5000 r/min, and the torque reference increases from 0 to 100 N $\cdot$ m. In Fig. 8, the voltage vector selection algorithm is applied without the d-axis current feedback. As shown in Fig. 8(a), the torque ripple reaches up to 270 N $\cdot$ m and the torque is not stabilized within 40 ms. The dq-axis current also oscillates under the fixed voltage angle shown from Fig. 8(b) and (e). This result agrees with the analysis of the root loci at $K_f = 0$

An effect of the d-axis current feedback is shown in Fig. 9. K_f and τ_f are 0.01 and 0.0004, respectively. A small oscillation is added to the voltage angle, as shown in Fig. 9(b). However, peak-to-peak torque ripple is reduced within 5 N $\cdot$ m, and the torque is also stabilized within 4 ms. The dq-axis current is also converged to the steady-state value and the current amplitude is around 156 A.

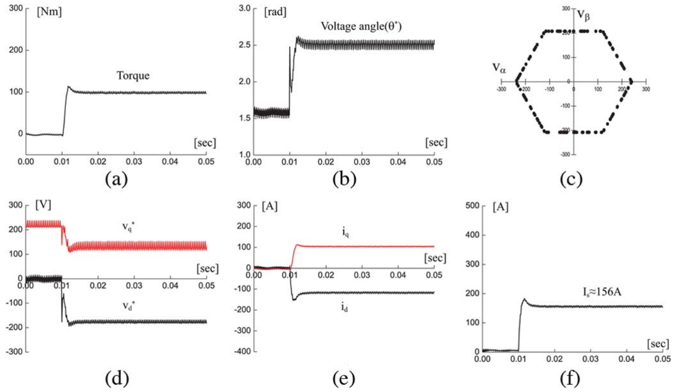

Fig. 9. Stepwise torque response (0 → 100 N · m) at 5000 r/min with the negative d-axis current feedback: (a) torque, (b) voltage angle(θ^*), (c) $\alpha\beta$-axis voltage, (d) dq-axis voltage, (e) dq-axis current, and (f) current amplitude.

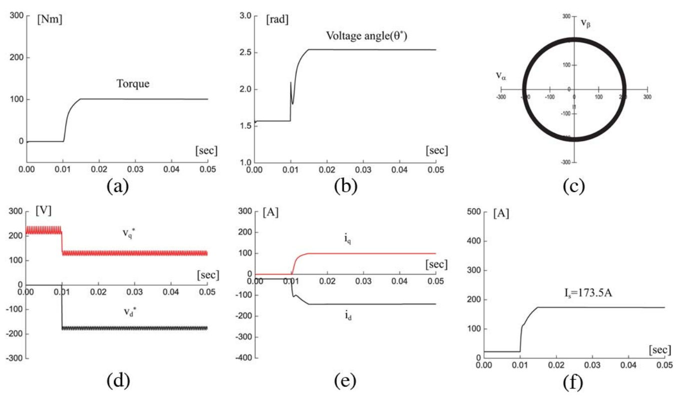

Fig. 10. Stepwise torque response (0 → 100 N · m) at 5000 r/min in the conventional current control with circular voltage limit: (a) torque, (b) voltage angle(θ^*), (c) $\alpha\beta$-axis voltage, (d) dq-axis voltage, (e) dq-axis current, and (f) current amplitude.

In Fig. 10, the torque control with the current vector control [3] is compared with the proposed algorithm under the same condition. As shown in Fig. 10(a) and (f), torque ripple is almost zero; however, the current amplitude is 173.5 A, which is larger than the one in Fig. 9 by 11.2%. Rising time of the torque is also longer than the proposed algorithm because the PI-type current controller causes an additional delay.

B. Experiment Results

In Fig. 11, stepwise response of torque and current of the proposed torque control algorithm is shown with various K_f: Fig. 11(a), (b) at $K_f = 0.005$, (c), (d) at $K_f = 0.075$ and (e), (f) at $K_f = 0.01$. The operating condition is the same as the simulation shown in Fig. 9, in which the speed is 5000 r/min and the torque command increases from 0 to 100 N · m. As shown in the effect of d-axis current feedback, when K_f increases, the torque overshoot decreases; however, the rising time increases. Torque ripple reduction is not outstanding when K_f increases. This is because the torque ripple at high speed is absorbed by the motor inertia.

In Fig. 12, the stationary frame voltage, (v_α, v_β) generated by the voltage vector selection algorithm are shown in the

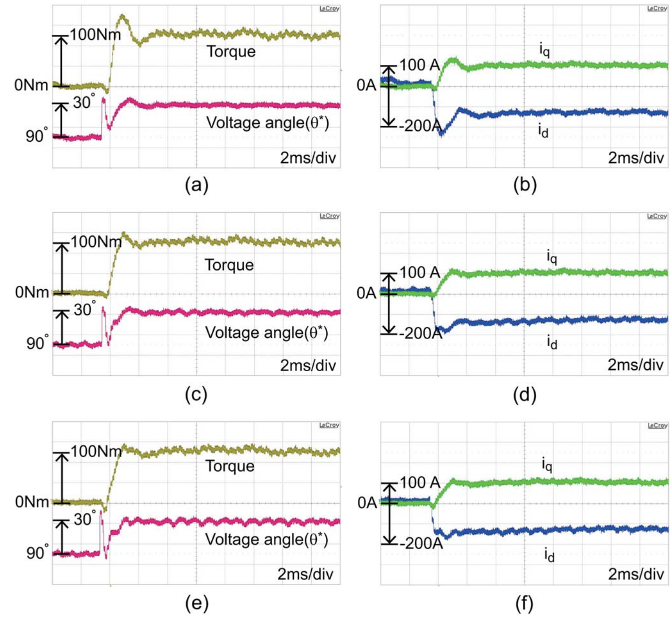

Fig. 11. Stepwise torque response (0 → 100 N · m) at 5000 r/min with various K_f: (a), (c), and (e) torque and voltage angle(θ^*); (b), (d), and (f) i_d and i_q; (a) and (b) at $K_f = 0.005$; (c) and (d) at $K_f = 0.075$; and (e) and (f) at $K_f = 0.01$.

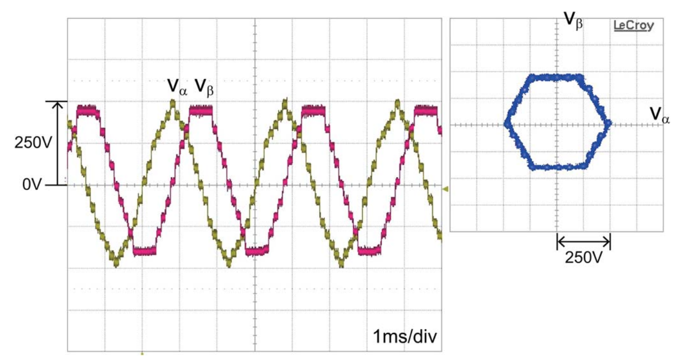

Fig. 12. Stationary frame voltage (v_α, v_β) on the hexagonal voltage limit.

steady sate. In the $v_\alpha - v_\beta$ plane, they form a hexagon of which the radius of the circumscribed circle is 240 V.

The same experiment is conducted by applying the current vector control. Because of the voltage saturation in the field weakening region, d- and q-axis current response represents nonlinear characteristics; rising time of the torque is lengthened compared with the one of the proposed algorithm, as shown in Fig. 13. In [15], the author showed increasing d-axis current by priority improved the current response in the field weakening region. The same effect is also shown in Fig. 11(b), (d), and (f).

Voltage, current, and power of Figs. 11 and 13 are shown in Fig. 14. These values are captured from the power meter. "U," "I" and "P" in the first column stand for voltage, current, and real power, respectively. In addition, "Element1" belongs to dc-link and "Σ A" corresponds to an average value of three phase output. As shown in Fig. 14(a), RMS line to line voltage of the inverter is 262.7 V, which corresponds to 214.5 V in terms of phase peak voltage. This value is smaller than the radius of the circumscribed circle (240 V) and larger than the one of

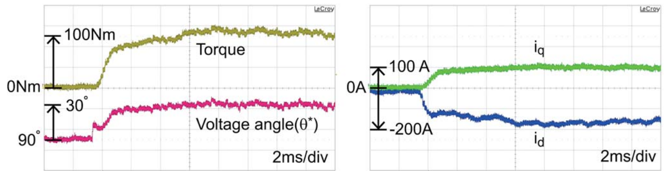

(a) (b)

Fig. 13. Stepwise torque response (0 → 100 N · m) at 5000 r/min in the conventional current control with circular voltage limit: (a) torque and voltage angle(θ^*), and (b) i_d and i_q.

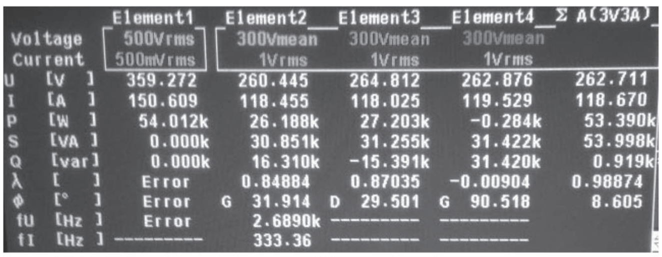

(a)

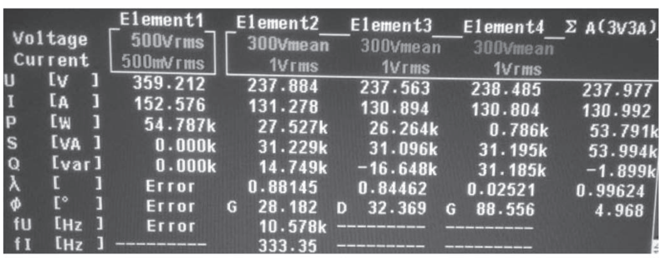

(b)

Fig. 14. Comparison of voltage (U), current (I), and power(P) under 100 N · m at 5000 r/min: (a) proposed torque control algorithm with hexagonal voltage limit. (b) current vector control with circular voltage limit.

the inscribed circle (207.8 V) of the hexagonal voltage limit. It increases by 10.39% compared with the value of the current vector control shown in Fig. 14(b). As a result, the phase current decreases by 9.4% and the real power of the inverter decreases by 400 W while generating the same torque.

In Table II, the phase voltage and current of the inverter are summarized in various operating conditions and the efficiencies of the motor and inverter are calculated based on measured power. "MotEff" and "InvEff" mean the efficiencies of the motor and inverter, respectively. In all conditions, the proposed torque control algorithm increases the voltage by 9.8% and decreases the current by 10.7% compared with the current vector control, on average. In addition, the efficiencies of the motor and inverter increases by 0.877% and 0.897%, on average. In terms of power, the proposed algorithm saves 312 W and 368 W, respectively. A reason for improvement of the inverter efficiency is due to switching loss reduction. Fig. 15 shows switching duties of each phase when the SVM is applied to the voltage vector shown in Fig. 12. It should be noted that each duty is fixed to one or zero for one third of one cycle of the electrical angle indicated by 360° in Fig. 15. It means that on–off switching always happened per one PWM period did not occur for two-thirds of one electrical angle period. This effect affects six switches of the inverter and improves the inverter efficiency.

TABLE II
PHASE VOLTAGE AND CURRENT OF INVERTER AND EFFICIENCIES OF MOTOR AND INVERTER. (a) PROPOSED TORQUE CONTROL. (b) CURRENT VECTOR CONTROL

(a)

Speed RPM	Torque Nm	V_{ph} V_{peak}	I_{ph} A_{peak}	MotEff %	InvEff %
12000	40	214.70	215.84	91.20	98.34
	20	216.04	181.58	84.51	97.45
8000	80	214.42	226.41	95.82	98.72
	50	215.34	163.47	95.31	98.58
	20	216.55	116.50	91.41	97.59
6000	100	214.63	205.76	96.92	98.79
	60	215.50	128.23	97.40	98.84
	30	216.16	74.20	96.31	98.67

(b)

Speed RPM	Torque Nm	V_{ph} V_{peak}	I_{ph} A_{peak}	MotEff %	InvEff %
12000	40	193.75	231.86	90.71	97.62
	20	196.57	196.24	82.43	96.35
8000	80	195.21	245.72	95.39	98.02
	50	196.44	179.18	94.93	97.80
	20	199.10	138.74	90.41	96.21
6000	100	195.09	224.66	96.58	98.10
	60	196.43	143.65	97.14	98.05
	30	197.61	92.20	94.28	97.66

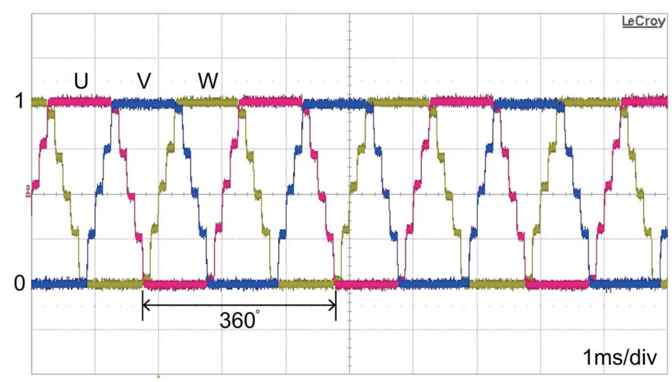

Fig. 15. U-, V-, and W-phase duties on the boundary of the hexagonal voltage limit.

VI. CONCLUSION

The torque control based on the voltage angle was proposed in this paper. It is different from previous works in that the hexagonal voltage limit is considered in the synchronous voltage plane to maximize the voltage utilization. The operating points are selected at the intersections between the sides of the rotating hexagon and the constant torque curves. From the simulation and experiment results, it was shown that the inverter output voltage increased and the phase current decreased, compared to when the circular voltage limit was utilized. As a consequence, the motor efficiency was improved. Moreover, the inverter efficiency was also increased owing to switching loss reduction. It was also shown via small-signal analysis that the d-axis current feedback with a high-pass filter results in stability.

The proposed algorithm was focused on the field weakening region only. In the low-speed region, the conventional method, such as the maximum torque per ampere, could be combined. In the future, the combining controller, which includes the transition method between low- and high-speed regions will be studied.

References

[1] K. H. Nam, *AC Motor Control and Electric Vehicle Applications*. Boca Raton, FL, USA: CRC Press, 2010.

[2] B. Cheng and T. R. Tesch, "Torque feedforward control technique for permanent-magnet synchronous motors," *IEEE Trans. Ind. Electron.*, vol. 57, no. 3, pp. 969–974, Mar. 2010.

[3] S.-Y. Jung, J. Hong, and K. Nam, "Current minimizing torque control of the IPMSM using Ferrari's method," *IEEE Trans. Power Electron.*, vol. 28, no. 12, pp. 5603–5617, Dec. 2013.

[4] S.-Y. Jung, J. Hong, and K. Nam, "Copper loss minimizing torque control of IPMSM based on flux variables," in *Proc. IEEE IEMDC*, May 2013, pp. 1174–1179.

[5] L. Zhong, M. F. Rahman, W. Y. Hu, and K. W. Lim, "Analysis of direct torque control in permanent magnet synchronous motor drives," *IEEE Trans. Power Electron.*, vol. 12, no. 3, pp. 528–536, May 1997.

[6] M. F. Rahman, L. Zhong, and K. W. Lim, "A direct torque-controlled interior permanent magnet synchronous motor drive incorporating field weakening," *IEEE Trans. Ind. Appl.*, vol. 34, no. 6, pp. 1246–1253, Nov./Dec. 1998.

[7] Y. Ren, Z. Q. Zhu, and J. Liu, "Direct torque control of permanent-magnet synchronous machine drives with a simple duty ratio regulator," *IEEE Trans. Ind. Electron.*, vol. 61, no. 10, pp. 5249–5258, Oct. 2014.

[8] S. Mathapati and J. Bocker, "Analytical and offline approach to select optimal hysteresis bands of DTC for PMSM," *IEEE Trans. Ind. Electron.*, vol. 60, no. 3, pp. 885–895, Mar. 2013.

[9] L. Tang, L. Zhong, M. F. Rahman, and Y. Hu, "A novel direct torque controlled interior permanent magnet synchronous machine drive with low ripple in flux and torque and fixed switching frequency," *IEEE Trans. Power Electron.*, vol. 19, no. 2, pp. 346–354, Mar. 2004.

[10] M. Preindl and S. Bolognani, "Model predictive direct torque control with finite control set for PMSM drive systems Part 1: Maximum torque per ampere operation," *IEEE Trans. Ind. Informat.*, vol. 9, no. 4, pp. 1912–1921, Nov. 2013.

[11] D. Stojan, D. Drevensek, Z. Plantic, B. Grcar, and G. Stumberger, "Novel field-weakening control scheme for permanent-magnet synchronous machines based on voltage angle control," *IEEE Trans. Ind. Appl.*, vol. 48, no. 6, pp. 2390–2401, Nov./Dec. 2012.

[12] H. Lee, J. Kim, J. Hong, and K. Nam, "Torque control for IPMSM in the high speed range based on voltage angle," in *Proc. IEEE APEC Expo.*, Mar. 2014, pp. 2500–2505.

[13] P.-Y. Lin and Y.-S. Lai, "Voltage control technique for the extension of DC-link voltage utilization of finite-speed SPMSM drives," *IEEE Trans. Ind. Electron.*, vol. 59, no. 9, pp. 3392–3402, Sep. 2012.

[14] S. Kim and J.-K. Seok, "Maximum voltage utilization of IPMSMs using modulating voltage scalability for automotive applications," *IEEE Trans. Power Electron.*, vol. 28, no. 12, pp. 5639–5646, Dec. 2013.

[15] J. Kim, S. Jung, and K. Nam, "Dynamic overmodulation in the synchronous reference frame for IPMSMs," in *Proc. ECCE*, Sep. 2012, pp. 815–822.

Sung-Yoon Jung received the M.S. and Ph.D. degrees in electrical engineering from Pohang University of Science and Technology, Pohang, Korea, in 2008 and 2013, respectively.

Since 2013, he has been a Postdoctoral Researcher with the University of Michigan, Dearborn, MI, USA. His research interests are design, analysis, and control of power electronic systems, ac motor drives, and electric vehicles.

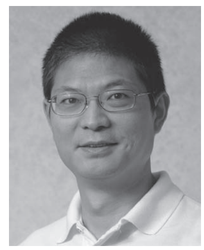

Chunting Chris Mi (S'00–AM'01–SM'03–F'12) received the B.S. and M.S. degrees from Northwestern Polytechnical University, Xi'an, China, and the Ph.D. degree from the University of Toronto, Toronto, ON, Canada, all in electrical engineering.

Previously, he was an Electrical Engineer with General Electric Canada, Inc. He is currently a Professor of electrical and computer engineering and the Director of the newly established Department of Energy GATE Center for Electric Drive Transportation, University of Michigan, Dearborn, MI, USA. He is the author of more than 100 articles. His research interests include electric drives, power electronics, electric machines, renewable-energy systems, and electrical and hybrid vehicles.

Kwanghee Nam (S'83–M'86) received the B.S. degree in chemical technology and the M.S. degree in control and instrumentation engineering from Seoul National University, Seoul, Korea, in 1980 and 1982, respectively, and the M.S. degree in mathematics and the Ph.D. degree in electrical engineering from The University of Texas at Austin, Austin, TX, USA, in 1986.

From 1998 to 2000, he was the Director of the Information Research Laboratories and the Dean of the Graduate School of Information Technology, Pohang University of Science and Technology (POSTECH), Pohang, Korea, where he is currently a Professor with the Department of Electrical Engineering. His current research interests include ac motor control, power converters, motor design, and electric vehicles. He is currently the Director of the POSTECH E-Car Research Center, developing electric power trains. He is the author of *AC Motor Control and Electrical Vehicle Applications* (CRC Press, 2010).

Prof. Nam was the recipient of the Best Transactions Paper Award from the IEEE Industrial Electronics Society in 2000 and a Second Best Paper Award at ECCE 2014.